Protections 2016 Ft. Collins, Colorado, USA, 7-9 September 2016
2nd International Seminar on
Dam Protection Against Overtopping
ISBN: 978-1-1889143-27-9 DOI:

Pressure and Velocity Distributions in Plunge Pools

Luis G. Castillo and José M. Carrillo
[1]Dept. of Civil Engineering
Universidad Politécnica de Cartagena (UPCT)
Paseo Alfonso XIII, 52, 30203 Cartagena
Spain
E-mail: luis.castillo@upct.es, jose.carrillo@upct.es

ABSTRACT

When dam overtopping produces rectangular free jets that discharge into plunge pool basins below the dam, the pressure and velocity distributions of the flow in the plunge pool must be estimated to evaluate potential scour that might destabilize the dam. The high turbulence and aeration phenomena that appear in falling jets and dissipation basins make it difficult to carry out studies based only on classical methodologies. This work addresses plunge pool flows, and compares numerical results against our own experiments. Instantaneous pressures, velocities and air entrainment were obtained with the use of piezoresistive transducers, Acoustic Doppler Velocimeter and optical fiber, respectively. Mean velocity field and turbulence kinetic energy profiles were determined. To identify the level of reliability of models, numerical simulations were carried out by using the "homogeneous" model of ANSYS CFX, together with different turbulence closures. The numerical results fall fairly close to the values measured in the laboratory, and with expressions for submerged hydraulic jumps and horizontal wall jets. The observations can be well predicted for horizontal velocities greater than 40% of the maximum velocity in each profile, and when the ratio of the water cushion depth to the jet thickness is lower than 20.

Keywords: *Air Entrainment, Free Falling Jets, Impingement Jets, Laboratory, Numerical Simulations, Overtopping.*

1. INTRODUCTION

In recent years, the increasing magnitude of design floods has prompted re-evaluations of spillway capacity and operational scenarios for large dams throughout the world. Current capacity of many spillways is inadequate, raising the possibility that dams might be overtopped during extreme events. This creates new loading scenarios for the dam and raises questions about erosion and scour downstream from the dam (Wahl et al. 2008, FEMA 2014).

When the rectangular jet or nappe flow occurs due to overtopping, the design considerations need to ensure that most energy is dissipated, and that there is minimal to no erosion downstream of the dam. In other words, we need to estimate the hydrodynamic actions on the bottom of the basin where the jet discharges, as a function of the characteristics of the jet (Annandale 2006). The energy dissipation mechanisms that occur in the jet-basin structure can be grouped into the following: (a) aeration and disintegration of the jet in its fall, (b) air entrainment and diffusion of the jet into the basin, (c) impact on the basin bottom, and (d) recirculation in the basin (Figure 1).

Two of the variables needed to be defined in the design of the jets are the issuance conditions and the impingement conditions.

Issuance conditions correspond to the flow conditions at a location where the jet leaves the spillway and starts falling freely. In the illustrated arch dam case with an inclined crest, $z = -h$, where z is the vertical coordinate with origin in the crest weir, and h is the weir head. Similarly, in the case of flat-topped case is also considered $z = -h$. The impingement conditions correspond to the jet section before the impact with the water surface of the basin. In this location, the mean velocity, V_j, and the impingement jet thickness, B_j, must be defined (see Figure 1).

This jet thickness must include the basic thickness due to gravity B_g, and the symmetric jet lateral spreading due to turbulence and aeration effects, ξ (Castillo et al. 2015):

$$B_j = B_g + 2\xi = \frac{q}{\sqrt{2gH}} + 4\varphi\sqrt{h}\left(\sqrt{2H} - 2\sqrt{h}\right) \quad (1a)$$

where q is the specific flow, H the fall height, and h is the energy head at the crest weir. $\varphi = K_\varphi T_u$, with T_u being the turbulence intensity (0.012 for inclined crest and 0.013 for a flat crest) and K_φ an experimental parameter (1.14 for circular jets, 1.24 for the three-dimensional nappe flow and 1.20 for the flat top case).

By the way, in the case of flat-topped dams the overtopping is produced on the crest of the dam through critical flow conditions. In the brink the depth is approximately 0.715 y_c (Rouse 1936 and Wahl et al. 2008). However, as already indicated, the issuance conditions are considered at z = - h. Figures 1a and 1b show the overtopping on an inclined-crest and a flat-crest dam, respectively. When the jet falls through a long-enough distance, the jet becomes fully developed (L_b).

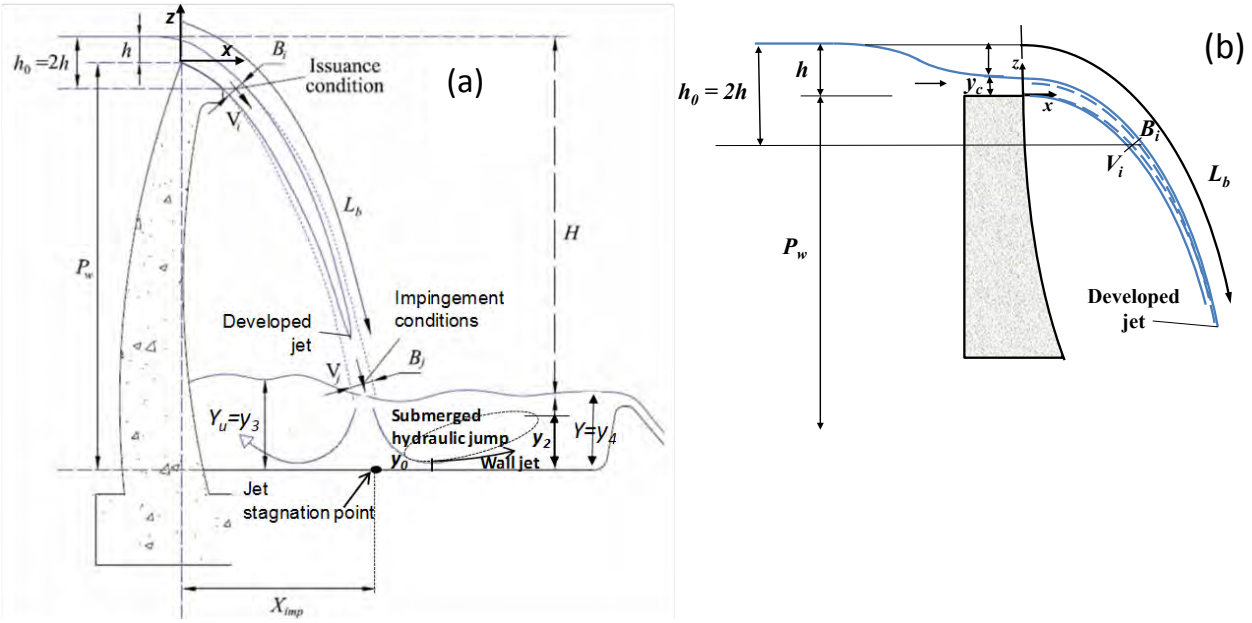

Figure 1. Schematic of falling rectangular jets and receiving basin. (a) Overtopping on an arch dam. (b) Overtopping on a gravity dam (flat top).

Castillo et al. (2015) established different equations to calculate the jet energy dissipation in the air and in the water cushion, as a function of the Y/B_j and H/L_b ratios (where Y and H denote the depth of the water cushion at the exit and the total head, respectively, and L_b is the break-up length). Castillo et al. (2015) proposed the following expression for estimating the break-up length:

$$\frac{L_b}{B_i F_i^2} = \frac{K}{(\varphi F_i^2)^{0.82}} \quad (1.b)$$

where B_i and F_i are the jet thickness and the Froude number in issuance conditions, respectively. K is an adjustment coefficient and that in the arch dam case is 0.85. If in the expression (1.b) we replacement the jet thickness $B_i = q / V_i$; velocity $V_i = 2\sqrt{gh}$; specific flow $q = h^{3/2} C_d$; Froude number $F_i = V_i/\sqrt{gB_i}$ and we solve for the break-up length, then it is obtained that:

$$L_b = \frac{C_d^{0.82} h^{0.73}}{2g^{0.68}\varphi^{0.82}} K \quad (1.c)$$

where C_d is the discharge coefficient (2.1 and 1.7 for arch dam and gravity dam (flat top), respectively).

Figure 2a show the sensitivity analysis of the K coefficient for a Turbulence index $T_u = 0.013$ (flat top case). We can observe that for $K = 1$ the break-up length is very similar to the inclined crest case ($T_u = 0.012$ and $K = 0.85$). Since in this case the turbulence index is somewhat greater than in the inclined crest case, then it seems reasonable that the length of disintegration is less. In this way was established $K = 0.95$. Figure 2b confirms that in the flat top case the initial conditions corresponding to $T_u = 0.013$ and $K = 0.95$.

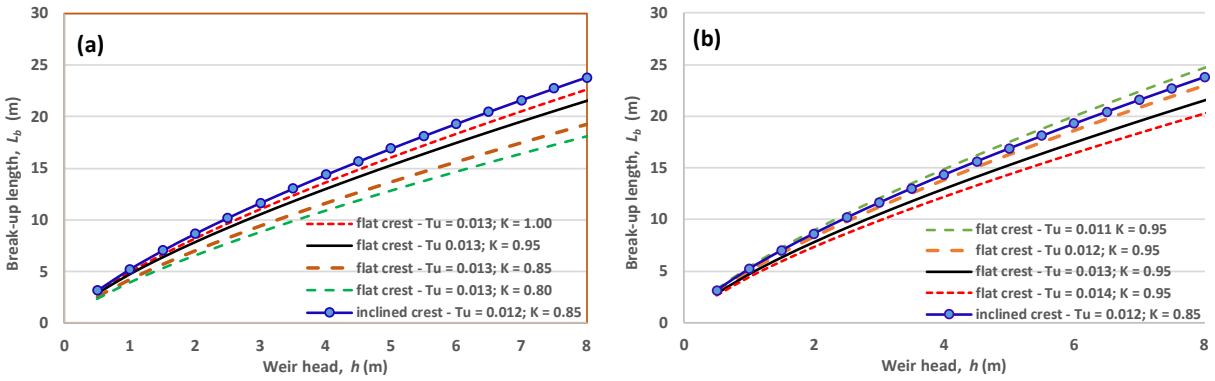

Figure 2. Break-up length in function of weir head for arch and gravity dams.

Figure 3 show the sensitivity analysis for K_φ parameter in function of relation H / h and $T_u = 0.013$. We can conclude that the jet expansion term for a flat crest case ($T_u = 0.013$ and $K_\varphi = 1.14$) is equal to the inclined case (($T_u = 0.012$ and $K_\varphi = 1.24$). However, the jet expansion term must should be slightly higher for the flat crest case so it was established that $K_\varphi = 1.20$ (intermediate value between a circular jet, $K_\varphi = 1.14$ and a nappe flow case, $K_\varphi = 1.24$).

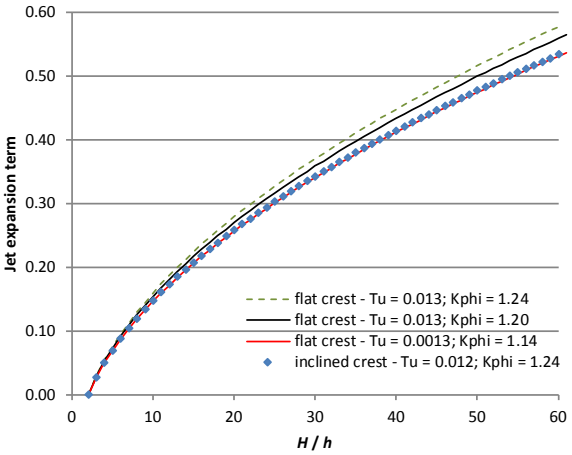

Figure 3. Jet expansion in function of the H/h relation and the K_φ parameter.

During the falling, the energy dissipation is due to the air entrainment into the falling jet and the depth of water upstream of the jet. In Figure 4, the velocity V_j and the jet thickness B_j at the impingement conditions, the core depth or minimum depth for effective water cushion and the two principal eddies that produce the dominant frequencies in the plunge pool (large scale eddies and shear layer structures) are sketched. The lowest frequencies correspond to large scale eddies that have a dimension on the order of the plunge pool depth. Then, the recirculating velocity for large plunge pools is about $V_r \sim 0.035\ V_j$ and the corresponding Strouhal number of the dominant eddies is $S = fY/V_j = (V_r/\pi Y)\ (Y/V_j) \sim 0.01$ (Ervine and Falvey 1987; Ervine et al. 1997). The following dominant frequency corresponds to eddy sizes contained in half of the shear-layer width and is proportional to the entry jet velocity; then, the Strouhal number of the shear-layer eddies is equal to a constant $S_s = (f_s Y/V_j) = K_3 \sim 0.25$, and it coincides with the spread of the jet into the water cushion as shown on Figure 4 (Ervine and Falvey 1987; Ervine et al. 1997).

Energy dissipation in the basin by diffusion effects can only be produced if there is an effective water cushion (Y/B_j > 5.5 for the rectangular jet case, Castillo et al. 2015). The instantaneous pressures signals obtained on the bottom of the plunge pools may be adjusted in curves for different ranges (see Figure 5).

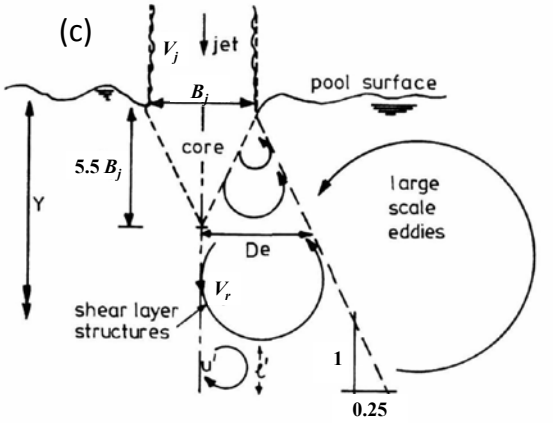

Figure 4. Eddy structures in effective water cushion ($Y \geq 5.5\ B_j$): large scale eddies size ~Y and shear layer structures size ~De (Castillo et al. 2016).

The dynamic pressure in the bottom of the stilling basin is based on two components: the mean dynamic pressure, C_p, (Figure 5a) and the fluctuating dynamic pressure, C_p', (Figure 5b). These dynamic pressure coefficients are used as estimators of the stream power reduction coefficients, by an effect of the jet disintegration in the air and their diffusion in the stilling basin. Hence, the dynamic pressures are also a function of the fall height to disintegration height ratio, H/L_b, and water cushion to impingement jet thickness, Y/B_j. Thus, the total dynamic pressure is expressed as:

$$P_{total} = C_p(Y/B_j)P_{jet} + FC_p'(Y/B_j)P_{jet} \quad (2)$$

where $C_p(Y/B_j)$ is the mean dynamic pressure coefficient; $C_p'(Y/B_j)$ the fluctuating dynamic pressure coefficient; P_{jet} the stream power per unit of area, and F the reduction factor of the fluctuating dynamic pressure coefficient. In rectangular jet case (nappe flow), Carrillo (2014) and Castillo et al. (2015) adjusted the formulae by using new laboratory data (Figure 5c).

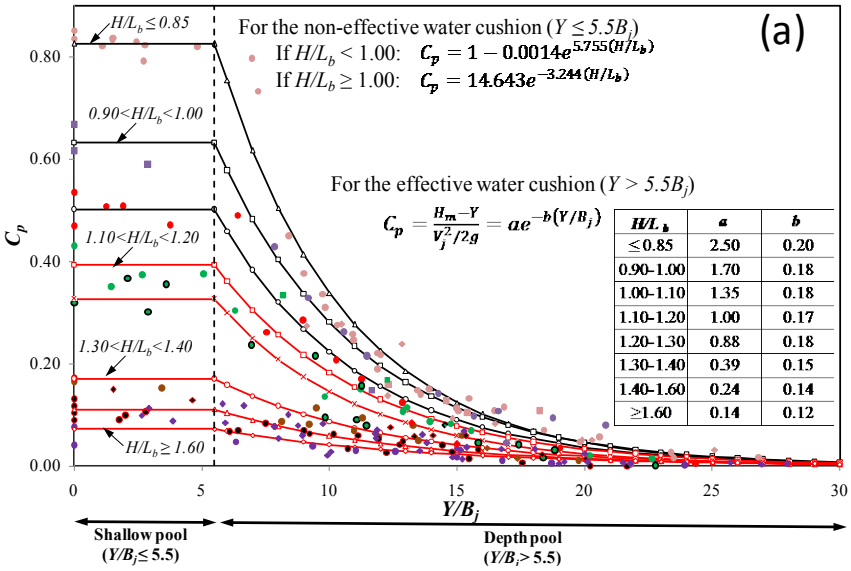

H/L_b	a	b
≤0.85	2.50	0.20
0.90-1.00	1.70	0.18
1.00-1.10	1.35	0.18
1.10-1.20	1.00	0.17
1.20-1.30	0.88	0.18
1.30-1.40	0.39	0.15
1.40-1.60	0.24	0.14
≥1.60	0.14	0.12

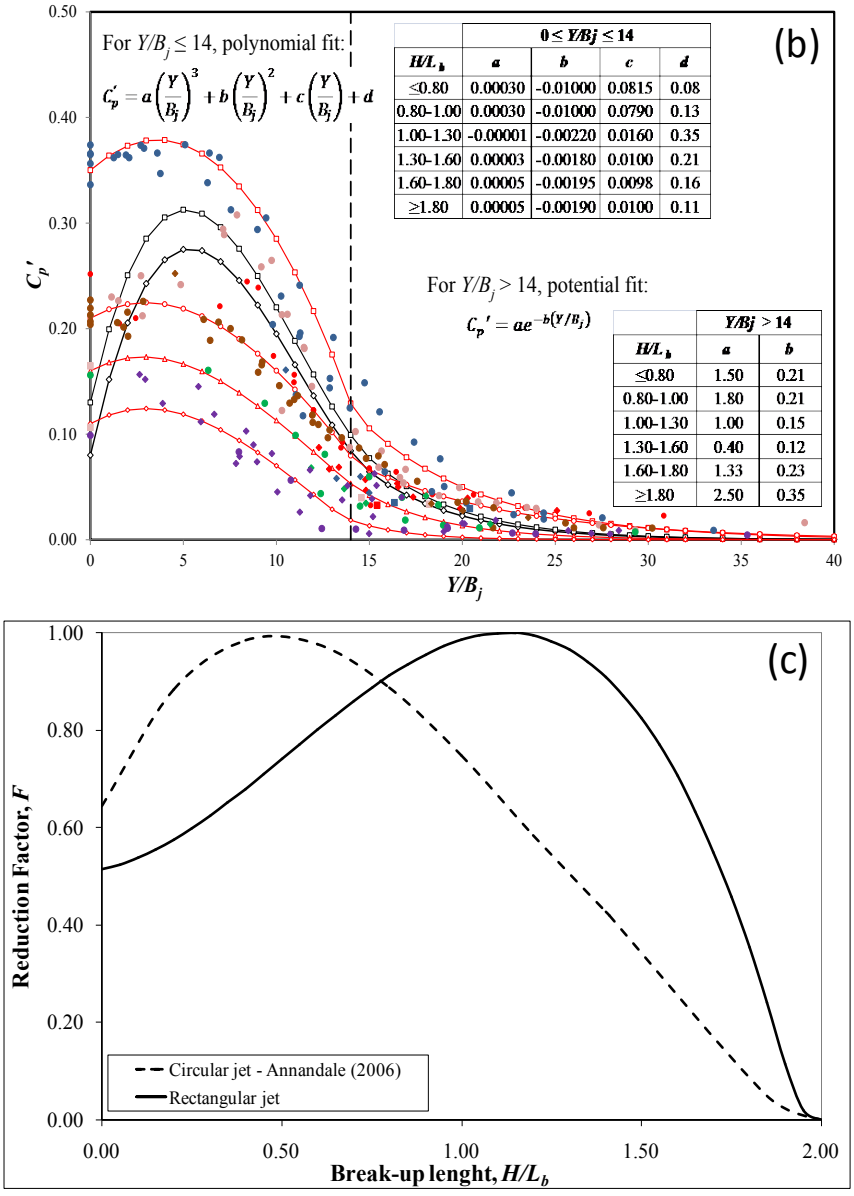

H/L_b	$0 \leq Y/Bj \leq 14$ a	b	c	d
≤0.80	0.00030	-0.01000	0.0815	0.08
0.80-1.00	0.00030	-0.01000	0.0790	0.13
1.00-1.30	-0.00001	-0.00220	0.0160	0.35
1.30-1.60	0.00003	-0.00180	0.0100	0.21
1.60-1.80	0.00005	-0.00195	0.0098	0.16
≥1.80	0.00005	-0.00190	0.0100	0.11

H/L_b	$Y/Bj > 14$ a	b
≤0.80	1.50	0.21
0.80-1.00	1.80	0.21
1.00-1.30	1.00	0.15
1.30-1.60	0.40	0.12
1.60-1.80	1.33	0.23
≥1.80	2.50	0.35

Figure 5. Pressure coefficients for the nappe flow case: (a) Mean dynamic coefficient, C_p. (b) Fluctuant dynamic coefficient, C_p'. (d) Reduction factor F of fluctuating dynamic coefficient.

Within the plunge pool downstream of the impingement point, the flow resembles a flow in a submerged hydraulic jump and a wall jet. However, the situation is complicated here by the air entrainment. Several formulas have been put forward to express the horizontal velocity distribution in the vertical direction. We return to some of these formulas later in the paper. In Castillo et al. (2014), the so-called "homogeneous" theoretical model of CFX was employed. It was shown that this model is able to reproduce correctly the jet water velocity, and the averaged pressures in the plunge pool. There is always a challenge in modeling two-phase flows to discern which level of complexity is needed to represent different aspects of the flow (Bombardelli and Jha 2009). One of the objectives of this paper is to determine whether this theoretical model is sophisticated enough to represent velocities in the plunge pool. Continuing the line of research, this work presents a systematic study which considers specific flows and water cushions in the plunge pool. New laboratory data were obtained and new three-dimensional simulations were specifically performed for this work. ANSYS CFX was again selected due to the variety of turbulence closures available in the code, the previous experience with it and, more importantly, due to the diverse two-phase flow models embedded in the package, which can allow us to expand the research further in the long-term future.

2. EXPERIMENTAL FACILITY

2.1. Turbulent Jet Experimental Facility

The experimental facility was constructed at the Hydraulics Laboratory of the Universidad Politécnica de Cartagena, and was described in detail in Carrillo and Castillo (2015). The facility consists of a mobile mechanism which permits to vary the weir height between 1.7 and 3.5 m, and flows from 10 to 150 l/s. It has an inlet channel with a length of 4.0 m and width of 0.95 m. The discharge is produced through a sharp-crested weir with a width of 0.85 m and height of 0.37 m. The plunge pool, in which different water cushions may be simulated, is a 1.3-m high, 1.1-m wide and 3.0-m long methacrylate box. Turbulent kinetic energy values at the inlet channel were obtained with an Acoustic Doppler Velocimeter (ADV); mean velocities and air concentrations in different sections of the falling jet were acquired with optical fiber instrumentation; and instantaneous pressure values were measured with piezoresistive transducers located on the basin bottom. In addition, ADV and optical fiber were used in the basin to obtain velocity and air concentration profiles, respectively, downstream of the impingement point. Figure 6a shows a picture of the experimental device in which sizable values of air concentration are apparent.

2.2. Optical Fiber Equipment

To measure the air concentration at the falling jet and at the basin, an RBI-instrumentation dual-tip probe optical fiber phase-detection instrument was used. This equipment enables measurement in water up to 20 m/s flow velocity and the relative uncertainty concerning the void fraction is estimated at about 15% of the measured value (Stutz and Reboud 1997). The rise and fall of the probe signal corresponds, respectively, to the arrival and the departure of the gas phase at the tip of the sensor. The void fraction was defined as the ratio of the total time the probe is in gas (Σt_{Gi}) to the experiment duration time t. Figure 6b shows the air concentration in different sections downstream of the jet stagnation point. The maximum air concentration is around 12% (at a distance of 21% from the bottom) for the first sections. However, from the section 0.30 m and a distance from the bottom smaller than 70%, the air concentration is below 10%. Concentrations remain high still at the upper portion of the water depth in the basin.

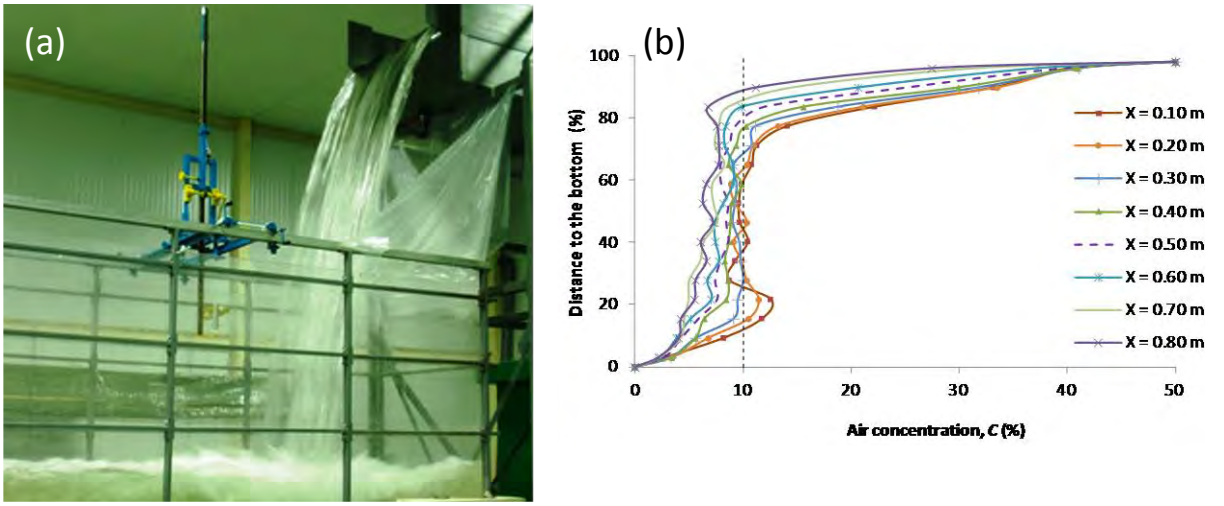

Figure 6. (a) Device of turbulent jets. (b) Air concentration in the basin for different sections downstream of the jet stagnation point. Measurements obtained by means of an optical fiber (q = 0.082 m^2/s, H = 2.19 m, and Y = 0.32 m).

2.3. Acoustic Doppler Velocimeter (ADV)

In order to characterize the macro turbulence of the flow in the plunge pool, 5000 values were recorded in each measured point by using a frequency of 10 Hz (more than eight minutes of observation). In this way, 2006 points in

the symmetrical vertical plane of the basin were obtained. As the flows are highly turbulent, the values obtained with ADV may be affected by spurious signals or "spikes". Furthermore, in this particular case, the air may also affect the signal of the ADV. Frizell (2000) experimented with the air effect, measuring concentrations varying from 0 – 3.61%. As the air concentrations increase and bubble sizes increase, correlation values drop dramatically as the acoustic signals used by the probe are absorbed and reflected by the two-phase flow mixture. Matos et al. (2002) also found that air bubbles affect the accuracy of velocity measurements taken with the ADV. However, their experimental results suggest that the ADV can provide reasonable estimates of the velocity for low air concentrations up to 8%.

3. MATHEMATICAL AND NUMERICAL MODELING

As can be seen from Figure 6, the flow conditions in the plunge pool are such that the air concentrations are relatively elevated at the point of jet impingement and nearby areas and in the top layer of the water depth. In these areas, there is a mostly non-dilute, two-phase flow. However, as we move far from the impingement point, the flow conditions tend to become quasi-dilute. That is why we decided to solve the equations for the conservation of mass and momentum for the mixture, which may be written in compact form (ANSYS CFX Manual 2015) as:

$$\frac{\partial(\rho\emptyset)}{\partial t} + \frac{\partial}{\partial x_j}\left[\rho U_j \emptyset - \Gamma \frac{\partial \emptyset}{\partial x_j}\right] = S \tag{3}$$

where ϕ is the transported quantity, i and j are indices which range from 1 to 3, x_i represents the coordinate directions (1 to 3 for x, y, z directions, respectively), and, t the time. In turn, $\rho = \sum_{k=1}^{Np} r_k \rho_k$, $U_j = \frac{1}{\rho}\sum_{k=1}^{Np} r_k \rho_k U_{kj}$, and $\Gamma = \sum_{k=1}^{Np} r_k \Gamma_k$, with r_k indicating the volume fraction of *k-th* fluid, Γ_k denoting the diffusion coefficient associated with the transported quantity for phase k, N_p denoting the number of phases and S indicating the sources/sinks for the transported quantity (ANSYS CFX Manual 2015). In this model, phases share the same velocity field. When $\phi = 1$, $S = 0$, and $\Gamma = 0$, the mass conservation equation is recovered, and when $\phi = U_i$, the momentum equation is recovered, with its corresponding source terms to account for the Reynolds stresses.

The theoretical model comes as a result of the addition of the equations of the two phases (Drew and Passman 1999; ANSYS CFX Manual 2015). Further, $\phi_K = \phi$. Rigorously speaking, models like this have been found to provide adequate predictions only in relatively-dilute mixtures. For larger concentrations they found that the velocity distribution could not be well predicted relatively far from the wall with mixture models. Thus, we expect the "homogeneous" model to be able to represent rather adequately those areas in which air concentrations are not that high. As said, the code ANSYS CFX has been used, which is based on an element-oriented, finite-volume method (FVM). It allows different types of volumes, including tetrahedral and hexahedral volumes. Solution variables are stored at the nodes (mesh vertices). More details are given in the ANSYS CFX Manual (2015).

3.1. Turbulence Models

In this work, one of the most usual two-equation turbulence models have been tested for the free falling jet and basin case. Two-equation models use the gradient diffusion hypothesis to relate the Reynolds stresses to the mean velocity gradients and the turbulent viscosity. The eddy viscosity hypothesis considers that eddies behave like molecules and the Boussinesq model assumes that the Reynolds stresses are proportional to the mean velocity gradients, as follows (Pope 2000):

$$-\rho\overline{u_i' u_j'} = \mu_t\left(\frac{\partial U_i}{\partial x_j} + \frac{\partial U_j}{\partial x_i}\right) - \frac{2}{3}\delta_{ij}(\rho k) \tag{4}$$

with μ_t being the eddy viscosity or turbulent viscosity, $k = 1/2(\overline{u_i' u_i'})$ is the turbulent kinetic energy and δ_{ij} the Kronecker delta. The *k-ω* based Shear-Stress Transport (SST) model (Menter 1994) assumes that the eddy viscosity is linked to the turbulence kinetic energy, k, and the turbulent frequency, ω, as $\mu_t = \rho\frac{k}{\omega}$. The SST model takes into

account the accuracy of the k-ω model in the near-wall region and the free stream independence of the k-ε model in the outer part of the boundary layer. It is considered as a hybrid model (see Rodi et al. 2012).

3.2. Free surface modeling

The Free Surface model assumes that each control volume contains three possible conditions:

- $r_k = 0$ if cell is empty (of the *k-th* fluid);
- $r_k = 1$ if cell is full (of the *k-th* fluid);
- $0 < r_k < 1$ if cell contains the interface between the fluids.

Tracking of the interface between fluids is accomplished by the solution of the volume fraction equation.

4. MODEL IMPLEMENTATION IN THREE DIMENSIONS

The model boundary conditions corresponded to the turbulence kinetic energy at the inlet obtained with ADV (located 0.50 m upstream of the weir), the upstream and downstream water levels and their hydrostatic pressure distributions. ANSYS CFX has different treatments near the wall. ω-based turbulence models (e.g. SST) use automatic wall functions which switch between regular wall functions (Pope 2000) and low-Reynolds wall treatment (Menter 1994). Considering the wall treatment used by ANSYS CFX, the mesh sizes close to the solid boundary were smaller than in the rest of the domain. Values of y^+ were smaller than 40. The symmetry condition in the longitudinal plane of the plunge pool was used.

The inlet condition considers the volumetric flow rate with a normal direction to the boundary (q = 0.082 m^2/s, q = 0.058 m^2/s, q = 0.037 m^2/s, q = 0.023 m^2/s) and the water level height at the upstream deposit (2.313 m for q = 0.082 m^2/s, 2.285 m for q = 0.058 m^2/s, 2.263 m for q = 0.037 m^2/s, 2.237 m for q = 0.023 m^2/s). The outlet condition was considered with flow normal to the boundary and hydrostatic pressure. The water level height at the outlet was modified according to the water cushion depth, Y, in the laboratory device. For all walls of the upper deposit, the weir and the dissipation basin, no slip smooth wall conditions were considered. The roughness of methacrylate was indicated in the walls. In the transverse direction, wall boundary conditions were used.

4.1. Mesh-Independence Tests

In Figure 7a, the simulations result for the different mesh sizes (5, 7.5, 10, 12.5 and 15 mm) in the free falling jet, obtained as a function of the vertical distance to the weir in terms of the flow velocities in the jet, are shown. Differences in velocities with the optical fiber measurement are smaller than 2% in all the cases (Castillo et al. 2014). From the analysis of Figure 7b, it can be concluded that mesh-independence is reached with an element size of 10 mm. The results are in agreement with previous results obtained on pressures at the stagnation point (Castillo et al. 2014). In this way, the mesh size of 10 mm seems to be valid for the flow rates analyzed.

4.2. Convergence Criteria

To judge the convergence of iterations in the numerical solution, we monitored the residuals. The solution is said to have converged in the iterations if the scaled residuals are smaller than fixed values ranging between 10^{-3} and 10^{-6}. In this work, the residual values were set to 10^{-4} for all the variables. With this choice and for 791,354 elements (255,776 in the falling jet), the mean computational time was 7.2×10^5 seconds (≈ 8.3 days), using a Central Processing Unit (CPU) with sixteen processors (Intel® Xeon® E5-2699 v3 @ 2.30 GHz).

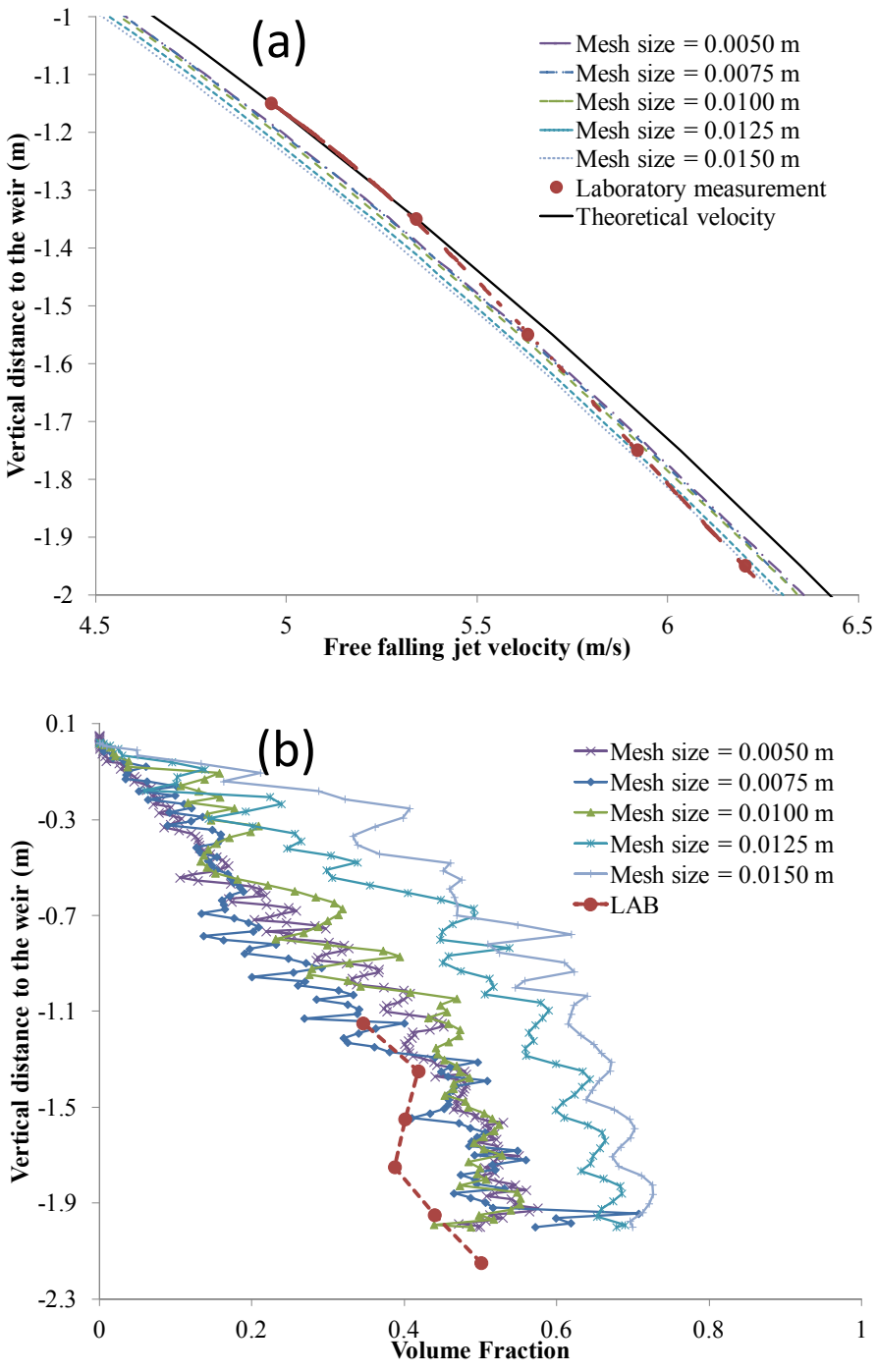

Figure 7. (a) Velocities and (b) Volume fractions as a function of the mesh size; q = 0.058 m2/s, h = 0.095 m.

5. RESULTS AND DISCUSSIONS

5.1. Velocity and Turbulent Kinetic Energy Distribution in the Plunge Pool

We can compare the velocity profiles in the forward flow if they are normalized with a velocity scale equal to the maximum velocity, V_{max}, at any section, and with a length scale δ_l equal to the elevation y from the bottom where the local velocity $V = V_{max}/2$, and the velocity gradient is negative (see Figure 8).

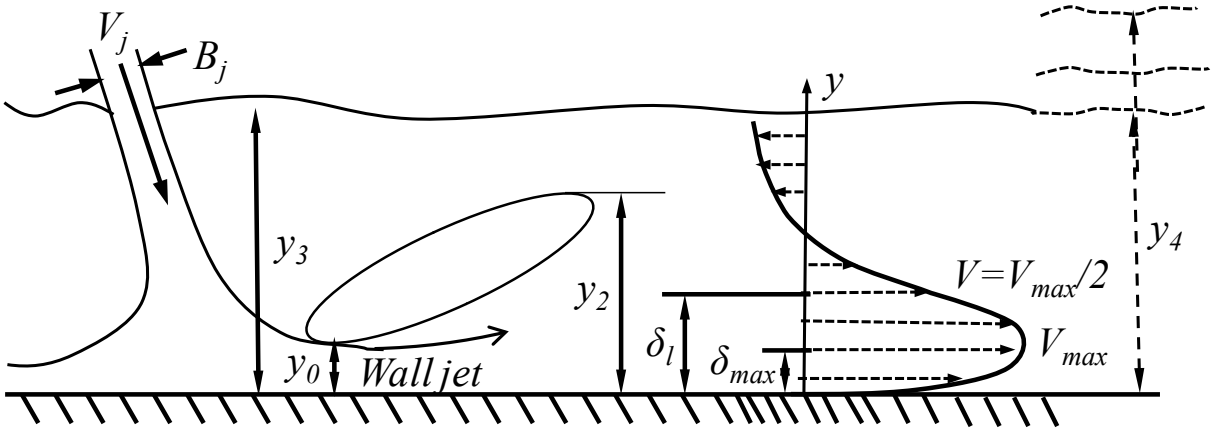

Figure 8. Velocity distribution sketch for submerged jumps (adapted from Wu and Rajaratnam 1996).

Velocities at different cross sections of the plunge pool located downstream of the stagnation point were measured with ADV. Results for the same cross sections were obtained from the CFD simulations (Castillo et al. 2016). The velocities have been made dimensionless by using the maximum horizontal velocities in each cross section, $V_{max,x}$ (Figure 9a). In addition to the mean velocities, the turbulent kinetic energy profiles were also compared (Figure 9b). In general, the results from the numerical simulations show the same behavior as the results obtained in the laboratory. Differences are important close to the stagnation point, where the numerical model may not obtain accurate results due to the relatively important air entrainment into the plunge pool (Figures 6a and 6b).

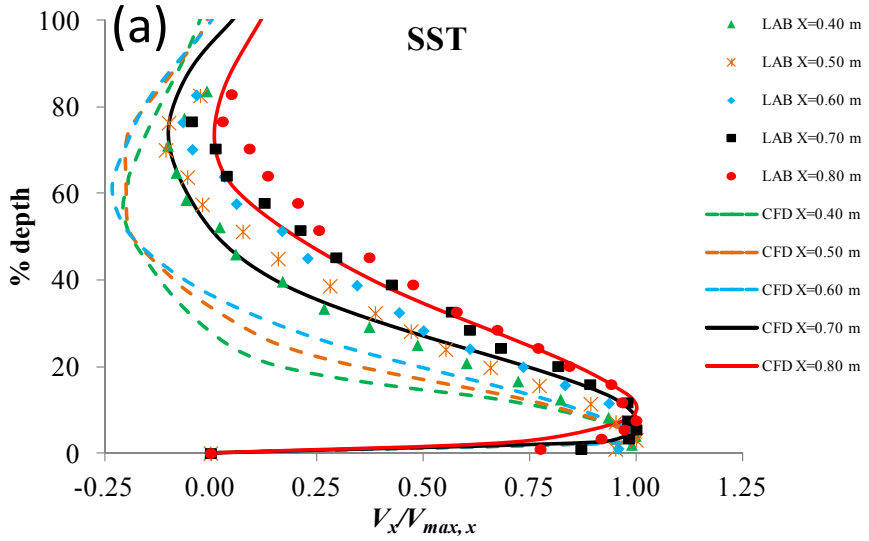

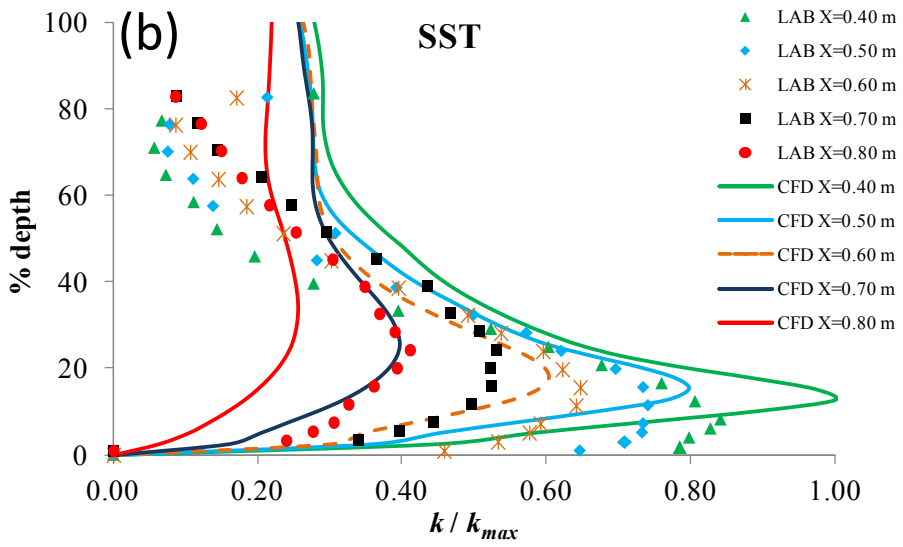

Figure 9. (a) Horizontal velocity profiles in the plunge pool downstream of the stagnation point. (b) Turbulent kinetic energy profiles. SST model (q = 0.082 m^2/s, H = 1.993 m, Y = 0.32 m).

Following Wu and Rajaratnam (1996), Figure 10a shows the results of the characteristic length obtained through the plunge pool. For each horizontal velocity profile measured with the ADV, the length scale δ_l was obtained in each section. Data have been classified as a function of the ratio water depth in the plunge pool/impingement jet thickness of each test. For ratios Y/B_j up to 20, the behavior is similar to that found in wall jets.

The values for water cushion depths Y/B_j up to 30 tend to fall within one standard deviation of the mean value. However, for larger water cushion depths, the characteristic length is higher. In this type of submerged hydraulic jump where the falling jet enters almost vertical, an equation may be obtained with the data that fall within one standard deviation of the mean value:

$$\frac{\delta_l}{B_j} = 0.465\frac{X}{B_j} + 2.415 \tag{5}$$

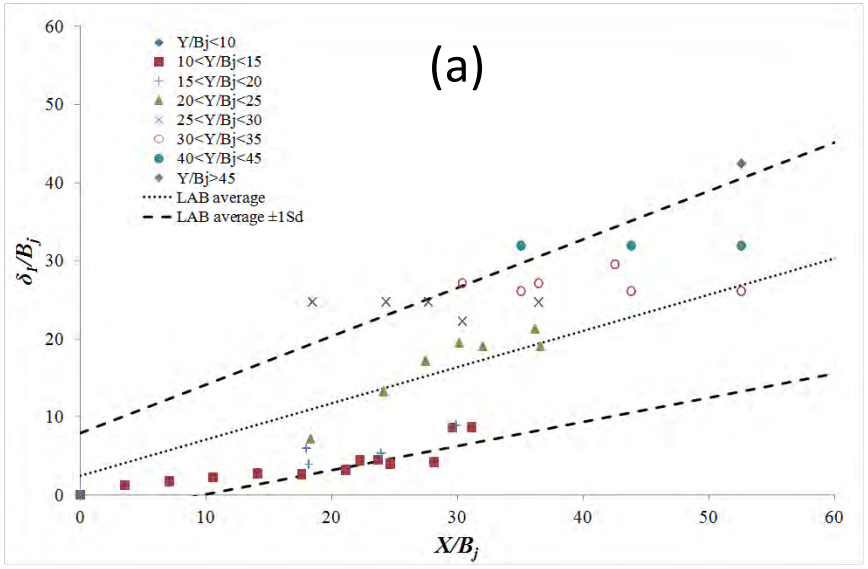

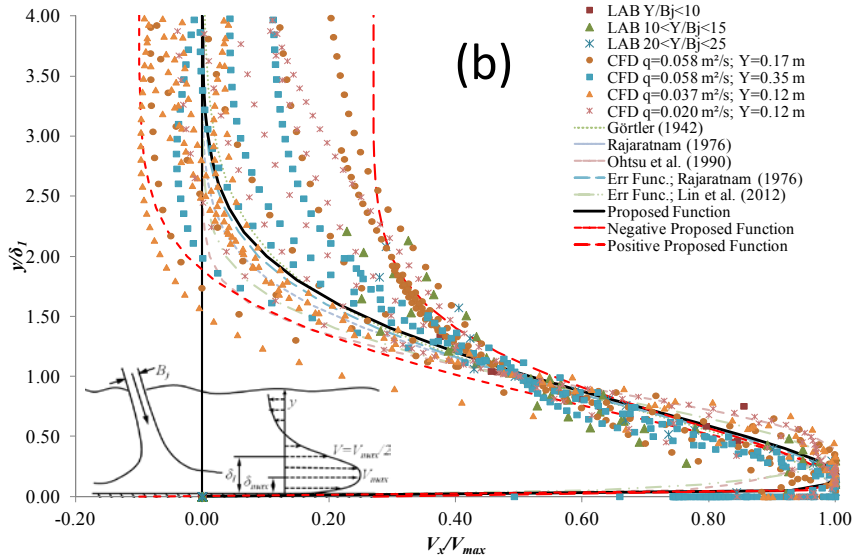

Figure 10. (a) Characteristic length δ_l in submerged hydraulic jumps. (b) Non-dimensional profiles of the horizontal velocity in the central vertical plane of the plunge pool.

Figure 10b shows the velocity profiles obtained from the numerical simulations as well as the laboratory measurements in the laboratory, together with equations proposed by diverse authors for horizontal wall jets (Castillo et al. 2016). The overall behavior of the observations can be predicted rather well by existing equations up to $y/\delta_1 \approx 1.5$. Disagreements appear when ratio $V_x/V_{max} < 0.4$. This seems to be related to the angle of impingement of the jet. In hydraulic jump studies, the wall jet is horizontal, while the impingement free falling jet enters almost vertical. The higher scatter occurs when the water cushion depth is $Y/B_j > 20$. In this way, the self-similarity disappears when the velocity profiles are close to the stagnation point and when a very submerged condition is obtained for the hydraulic jump. With all data, a new regression is proposed for submerged hydraulic jumps downstream of the impingement point:

$$\frac{V_x}{V_{max}} = 1.48 \left(\frac{y}{\delta_l}\right)^{1/7} \left(1 - erf\left(0.66 \frac{y}{\delta_l}\right)\right) \tag{6}$$

This proposed function is the separation line between the profiles in which there is negative recirculation flow and the profiles in which the flow is moving towards downstream.

For the range of flows and water cushions analyzed, the limit between both behaviors seems to be located at 0.2-0.3 m downstream of the stagnation point.

$$\frac{V_x}{V_{max}} = 1.65 \left(\frac{y}{\delta_l}\right)^{1/7} \left(1 - erf\left(0.72 \frac{y}{\delta_l}\right)\right) - 0.10 \tag{7}$$

$$\frac{V_x}{V_{max}} = 1.10 \left(\frac{y}{\delta_l}\right)^{1/7} \left(1 - erf\left(0.80 \frac{y}{\delta_l}\right)\right) + 0.27 \tag{8}$$

5.2. Energy dissipation in the plunge pool

In a horizontal channel, the total energy variation between the sections located upstream and downstream of the submerged hydraulic jump are, by definition:

$$H_L = \left(\frac{V_j^2}{2g} + y_3\right) - \left(\frac{V_4^2}{2g} + y_4\right) \tag{9}$$

where y_3 and y_4 are the water depths upstream and downstream of the submerged hydraulic jump generated by the jet. By using Eq. (9) with the continuity equation, the energy dissipation may be obtained as (Othsu et al. 1990)

$$\frac{H_L}{H_0} = \frac{2\left(\frac{y_3}{y_0} - \frac{y_4}{y_0}\right) + \left(1 - \frac{1}{(y_4/y_0)^2}\right)F_{r0}^2}{2\left(y_3/y_0\right) + F_{r0}^2} \tag{10}$$

where H_0 is the energy upstream of the hydraulic jump, and y_0 and F_{r0} the water depth and Froude number in the upstream section of the hydraulic jump. When $y_3 = y_0$ and $y_4 = y_2$, the free hydraulic jump expression is recovered.

Figure 11a shows the contrast between the relative energy dissipation and the Froude number at the jet impingement condition, $F_j = V_j/\sqrt{gB_j}$, obtained from experiments. In addition, results coming from the use of Eq. (10) have been included as a function of the ratio between the upstream water depth and the impingement jet thickness (y_3/B_j). In the laboratory device, the impingement Froude number is between 13 and 20 for the impingement jet thickness of 0.015 m plotted in Figure 11b. In general, tests carried out show an energy dissipation larger than 75% of the impingement jet energy. This ratio increases when the ratio y_3/B_j decreases (Castillo et al. 2016).

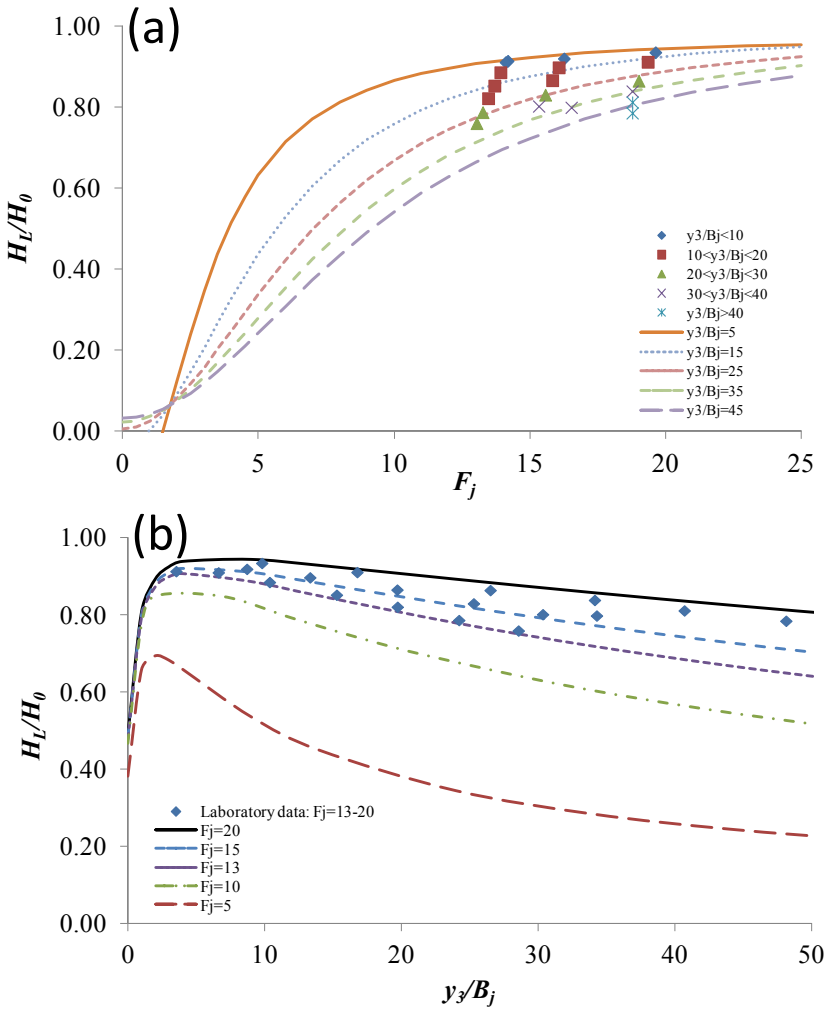

Figure 11. Relative energy dissipation in the plunge pool: (a) in function of the impingement Froude number. (b) in function of the ratio y_3/B_j for the cases B_j = 0.015 m and F_j = 13-20.

6. CONCLUSIONS

Observing and predicting two-phase flows in hydraulic structures is very complicated due to the rather non-dilute nature of the flow. Under non-dilute conditions, both experiments and simulations cannot be expected to lead to clean comparisons. In this work, mean velocity and turbulent kinetic energy profiles have been analyzed in a plunge pool located downstream of a rectangular free-falling jet. In general, the CFD simulations provided results fairly close to the values measured in the laboratory, and to the formulas proposed by diverse authors, in spite of having used a simple two-phase flow model. "Homogeneous" model seems to be able to predict rather well areas in which air concentration is not very high. However, in the highly aerated regions rather strong differences appear.
It was possible to propose a single mean velocity distribution law for ratios $V_x/V_{max} \geq 0.40$. For smaller values, there are necessarily diverse distribution laws.

7. ACKNOWLEDGEMENTS

The researchers express their gratitude to the financial aid received from the Ministerio de Economía y Competitividad (Spain) and the Fondo Europeo de Desarrollo Regional (FEDER), through the Natural Aeration of Dam Overtopping Free Jet Flows and its Diffusion on Dissipation Energy Basins project (BIA2011-28756-C03-02).

8. REFERENCES 2

Annandale, G.W. (2006). Scour Technology. McGraw-Hill Professional, NY, USA.
ANSYS, Inc. (2015). *ANSYS CFX. Reference Guide. Release 16.0*.
Bollaert, E.F.R. and Schleiss, A.J. (2003). "Scour of rock due to the impact of plunging high velocity jets Part I: A state-of the-art review." *J. Hydraulic Res.,* 41(5), 451-464.
Bombardelli, F.A. and Jha, S.K. (2009). "Hierarchical modeling of the dilute transport of suspended sediment in open channels." *Environmental Fluid Mechanics,* 9, 207-235.
Carrillo, J.M. (2014). Metodología numérica y experimental para el diseño de los cuencos de disipación en el sobrevertido de presas de fábrica. PhD Thesis. Departamento de Ingeniería Civil, Universidad Politécnica de Cartagena, Spain. [in Spanish].
Carrillo, J.M. and Castillo, L.G. (2015). "Laboratory measurements and numerical simulations of overtopping nappe impingement jets." *Dam Protections against Overtopping and Accidental Leakage - Proceedings of the 1st International Seminar on Dam Protections Against Overtopping and Accidental Leakage*, Madrid, Spain.
Castillo, L.G. and Carrillo, J.M. (2013). "Analysis of the scale ratio in nappe flow case by means of CFD numerical simulation." *Proc. 35th IAHR World Congress*, Chengdu, China.
Castillo, L.G., Carrillo, J.M. and Sordo-Ward, A. (2014). "Simulation of overflow nappe impingement jets." *J. Hydroinformatics*, 16(4), 922-940.
Castillo, L.G, Carrillo, J.M. and Blázquez, A. (2015). "Plunge pool dynamic pressures: a temporal analysis in the nappe flow case." *J. Hydraulic Res*., 53(1), 101-118.
Castillo, L.G, Carrillo, J.M. and Bombardelli, F.A. (2016). "Distribution of mean flow and turbulence statistics in plunge pools." *J. Hydroinformatics*. HYDRO-D-16-00044 (In Press).
Drew D. A. and Passman S. L. (1999). "*Theory of Multicomponent Fluids.*" Applied Mathematical Sciences. Volume 135. Springer New York.
Ervine, D.A. and Falvey, H.R. (1987). "Behaviour of turbulent water jets in the atmosphere and plunge pools." *Proc. Int. Conf. Institutions of Civil Engineers*, 83(2), 295-314.
Ervine, D. A., Falvey, H. T. and Withers, W. A. (1997). "Pressure fluctuations on plunge pool floors." *J. Hydraul. Res.,* 35(2), 257–279.
FEMA (2014). Technical Manual: Overtopping Protection for Dams. Federal Emergency Management Agency. FEMA P-1014, May. US Department of Homeland Security. USA.
Frizell, K.W. (2000). Effects of aeration on the performance of an ADV. *In: 2000 Joint Conf. on Water Resources Engineering and Water Resources Planning & Management.* ASCE. Hotchkiss, R.H., Glade, M. (Eds.), Minneapolis, USA (CD-ROM).
Matos, J., Frizell, K.H., Andre, S. and Frizell, K.W. (2002). On the performance of velocity measurement techniques in air-water flows. *In: Hydraulic Measurements and Experimental Methods Conference 2002*. ASCE. Wahl, T.L.,

Pugh, C.A., Oberg, K.A. and Vermeyen, T.B. (Eds.). Estes Park, CO, USA.
Menter, F.R. (1994). "Two-equation eddy-viscosity turbulence models for engineering applications." *AIAA J.,* 32(8), 1598-1605.
Ohtsu, F., Yasuda, Y. and Awazu, S. (1990). Free and submerged hydraulic jumps in rectangular channels. Report of the Research Institute of Science and Technology. Nihon University. No 35.
Pope, S. B. (2000). Turbulent flows. Cambridge University Press.
Rodi, W., Constantinescu, C. and Stoesser, T. (2012). Large-Eddy Simulation in Hydraulics. IAHR Monograph, CRC Press.
Rouse, H. (1936). Discharge Characteristics of the Free Over Fall (Rouse, Civil Engineering).
Stutz, B. and Reboud, J. L. (1997). "Two-phase flow structure of sheet cavitation." *Phys. Fluids,* 9(12), 3678–3686.
Wahl, T.L., Frizell, K.H. and Cohen, E.A. (2008). "Computing the trajectory of free jets." *J. Hydraul. Eng.,* 134(2), 256-260.
Wu, S. and Rajaratnam, N. (1996). "Free jumps, submerged jumps and wall jets." *J. of Hydraulic Research*, 33(2), 197-212.